Batteries & Supercaps

Articles
doi.org/10.1002/batt.202000112

Chemistry
Europe
European Chemical
Societies Publishing

Design of Highly Reversible Zinc Anodes for Aqueous Batteries Using Preferentially Oriented Electrolytic Zinc

Ehsan Faegh,[a] Benjamin Ng,[a] Dillon Hayman,[a] and William E. Mustain*[a]

Rechargeable zinc-based batteries have attracted a growing interest due to their intrinsic safety, low environmental impact and potentially very low cost. However, there still remains significant hurdles to achieve cells of commercial interest. Conventional commercial Zn anodes are formed from large, polycrystalline particles with limited control over the shape and size. In this study, preferentially oriented electrolytic Zn (e-Zn) particles with hexagonal shape and controlled size (~100 μm) were synthesized and physically characterized by SEM, XRD and BET techniques. The corrosion, discharge and cycling behavior of e-Zn particles were analyzed in KOH alkaline media. It was found that preferentially oriented e-Zn particles with low surface area have lower corrosion than Zn powder and 99% reduced corrosion rate with respect to polycrystalline Zn wire. Furthermore, e-Zn electrodes were successfully scaled up and showed remarkable reversibility in symmetric cells at a high rate of 20 mA cm^{-2} for 640 h. e-Zn/KOH/MnO$_2$ full cells were also demonstrated with ca. 6 times longer cycle life than Zn powder with a lower H$_2$ gassing rate at 10% Zn DoD and C/20 rate. In addition, a comparison between alkaline vs. mild acidic electrolyte was made in terms of reversibility and structural changes of preferentially oriented e-Zn electrodes where superior cycling was observed in ZnSO$_4$ for 2000 h.

1. Introduction

Today, Li-ion batteries dominate the secondary battery market because of their exceptional cycling performance, high energy density, and longevity.[1] However, safety and high cost are major concerns in Li-ion batteries, especially for emerging electric vehicle and grid storage applications, due to the use of flammable non-aqueous electrolytes and some toxic elements such as cobalt.[2–4] Among non-Li battery systems, Zn-based batteries have been touted as a promising option to compete with Li-ion batteries. Zn anodes have been a reliable electrode material in primary batteries since the 1960s due to their intrinsic safety, low cost of Zn metal and use of aqueous, non-flammable electrolytes. In addition, Zn has relatively high theoretical gravimetric (820 mAh g^{-1}) and volumetric capacity (5857 mAh cm^{-3}), which has made Zn-based electrodes attractive for use in secondary battery applications, especially for large-scale energy storage. However, the cycling performance of Zn electrodes has been limited by multiple challenges including passivation, shape change, dendrite formation, and corrosion (accompanied by hydrogen gas evolution) – especially in alkaline electrolytes.[5–8] An illustration of these phenomena is shown in Figure 1. The combination of these challenges with Zn electrodes leads to serious limitations including poor voltage reversibility and rapid capacity fade.

During discharge in KOH-based alkaline electrolytes, Zn is first electrochemically oxidized to zincate anions [Equation (1)].

However, the solubility of zincate is limited, and once the saturation concentration of zincate is reached ZnO is formed via a dehydration reaction [Equation (2)]. The formed ZnO passivates the surface, creating an insulating layer of porous cubic-rod shaped ZnO structures that: 1) restricts the accessibility of the electrolyte to the active Zn surface; 2) increases the cell impedance; and 3) limits the cell capacity by reducing the Zn utilization. Shape change occurs due to the non-uniform current distribution throughout the anode, as well as the non-uniform reaction across the Zn surface. This is also an issue when Zn-based materials are being recharged, where the non-uniform current density can result in the formation of dendrites. Zn dendrites initiate from regions on the surface where high local currents and high Zn concentrations dominate.[9] Zn dendrites can penetrate through the separator and cause short circuit and cell failure, although the recent development of 'water-in-salt' electrolytes with high voltages in aqueous batteries could suppress Zn dendrite formation.[10–13] Finally, Zn corrosion in alkaline media is thermodynamically favorable, since Zn oxidation [Equation (1)] has a more negative redox potential than the alkaline reduction of water [Equation (3)]. Therefore, spontaneous Zn corrosion occurs, coupled with H$_2$ gas evolution, Equation (4). Such H$_2$ gassing can cause an increase in the cell pressure that can sacrifice the integrity of primary cells[14] and lower the coulombic efficiency in secondary cells.
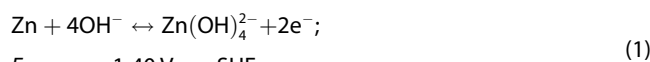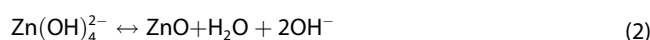
[a] E. Faegh, B. Ng, D. Hayman, W. E. Mustain
Department of Chemical Engineering,
University of South Carolina,
Columbia, South Carolina 29208, USA
E-mail: mustainw@mailbox.sc.edu

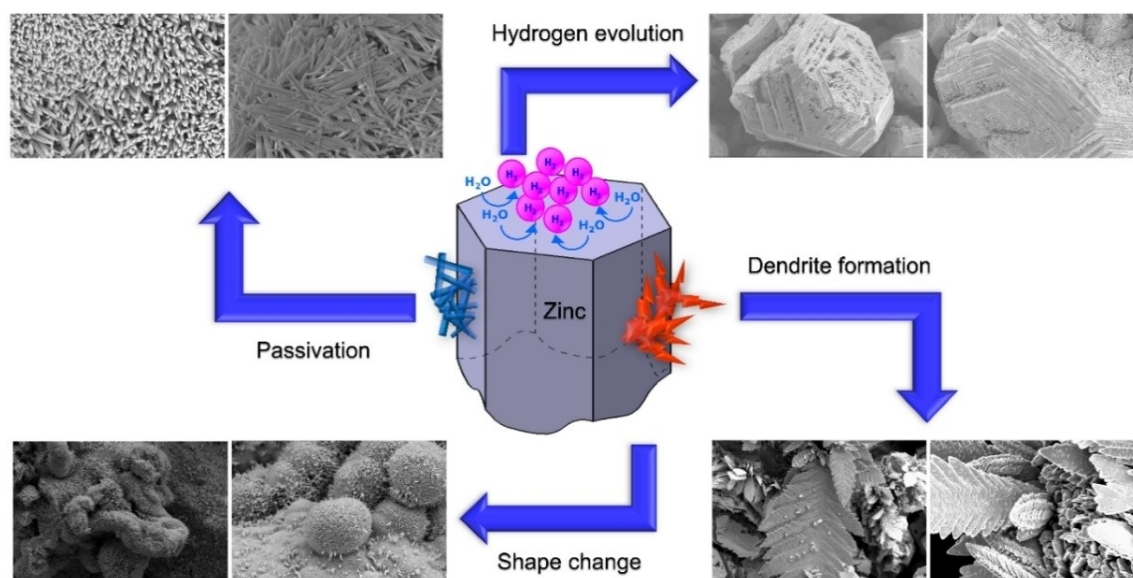Supporting information for this article is available on the WWW under
https://doi.org/10.1002/batt.202000112

$$Zn + 4OH^- \leftrightarrow Zn(OH)_4^{2-} + 2e^-;$$
$$E_{Nernst} = -1.40 \text{ V vs. SHE} \tag{1}$$

$$Zn(OH)_4^{2-} \leftrightarrow ZnO + H_2O + 2OH^- \tag{2}$$

$$2H_2O + 2e^- \rightarrow H_2 + 2OH^-;$$
$$E_{Nernst} = -0.92 \text{ V vs. SHE} \tag{3}$$

Figure 1. Illustration of Zn electrode challenges in alkaline battery applications.

$$Zn + 2OH^- + 2H_2O \leftrightarrow Zn(OH)_4^{2-} + H_2 \qquad (4)$$
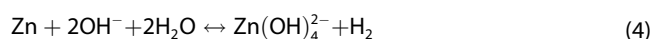
Particular to secondary cells, the inherent drawbacks of Zn have restricted their practical application. Because of this, in recent years, researchers have made significant efforts to overcome these challenges by managing the electrolyte using additives,[6,15–18] alloying and doping of Zn with other metals[19–21] as well as modifying the Zn electrode architecture, such as designing 3D electrodes.[22–29] For example, Parker and co-workers designed a 3D monolithic and porous Zn anode (Zn sponge) that was able to recharge over more than 100 cycles at 40% Zn depth of discharge (DoD).[22–23] The 3D architecture was able to improve the reaction uniformity and mitigate the shape change over long-term cycling. However, due to their high surface area, the Zn sponges were susceptible to corrosion and H_2 gassing, which is a disadvantage for practicality because of reduced shelf-life. This is a good example of the tradeoffs that Zn researchers have encountered within nearly every study. Practical solutions have the difficult requirement that all of the above challenges must be addressed simultaneously while also considering the cost of producing the materials and architectures of interest.

Traditional Zn anodes in alkaline batteries are formed from large, polycrystalline particles with limited control over the morphology. Some studies have looked to improve morphology control of Zn through the design of Zn nanostructures,[29–32] but the future realization of these nanomaterials is hampered by the high rate of corrosion for Zn nanostructures as well as the expense and scalability of manufacturing such nanostructures.[5,14] More importantly, it should be noted that an individual Zn particle is not an infinite single-crystal surface; real particles are inherently polycrystalline where multiple crystallographic facets and defects are exposed to the electrolyte. Since the adsorption of water and the surface electron density is different for each crystallographic Zn facet, the reaction free energy – and hence reversible potential – for both Zn dissolution [Equation (1)] and H_2 evolution [Equation (3)] reactions is orientation dependent. Thus, each of these contributes to the stability of Zn in alkaline media in a different manner, and the shape and size of the Zn particles can play an important role in its corrosion rate as well as its charge/discharge kinetics. For example, Won et al. showed that H_2 evolution is most favorable on the Zn (101) facet.[33] Therefore, it is essential to understand which orientation of Zn is optimal from the perspective of balancing corrosion and charge/discharge rates, which translate directly to practical variables such as shelf-life and achievable capacity.

Currently, the majority of researchers working on Zn-ion (as well as Zn-air) batteries focus on developing new cathode materials and simply apply Zn foil anodes. However, recent review articles have pointed to the need for increased attention to the Zn anode,[8,34–36] where the introduction of novel structures/architectures could have a significant effect and pave the way for the research community to seek new methods to overcome the Zn anode challenges and use the knowledge to implement in Zn-ion batteries with slightly acidic electrolyte. The same can be said for the Zn anode in conventional alkaline electrolytes as well. In other words, there is a gap in the field on understanding the effect of Zn surfaces and crystallographic orientations on the corrosion and electrochemical oxidation/reduction of Zn in both alkaline and mild acidic media.

Therefore, in the present study, micron-sized preferentially oriented electrolytic Zn (e-Zn) particles were synthesized through a facile electrodeposition method in a $ZnSO_4$ electrolyte without any additives at high current densities to investigate their surface stability and reversibility in alkaline media. The effect of electrodeposition parameters, such as substrate (Ni vs. Al) and current density on the growth and morphology of Zn were analyzed. The crystallography of the e-Zn surfaces was also manipulated using heat-treatment. In

Batteries & Supercaps

Articles
doi.org/10.1002/batt.202000112

Chemistry
Europe
European Chemical
Societies Publishing

addition, large-scale implementation of e-Zn particles was performed on mesh substrates and a novel design of Zn electrodes was proposed and tested in both symmetric cells as well as e-Zn/KOH/MnO$_2$ full cells. Moreover, H$_2$ gas evolution was monitored in real time during cycling of e-Zn/KOH/MnO$_2$ cells. Finally, the structural and electrochemical reversibility of e-Zn electrodes were evaluated in mild ZnSO$_4$ media that is similar to the electrodeposition environment and compared with alkaline KOH. ZnSO$_4$ has been proposed as a mildly acidic electrolyte to overcome the limitations of Zn in strongly alkaline pH as well as an enabling reaction media for Zn-ion batteries.

Experimental Section

Electrodeposition of e-Zn on wire substrates

e-Zn particles were synthesized in a custom-built three-electrode electrochemical cell at room temperature using an Autolab M101 potentiostat. Ni wires (1.0 mm dia, 99.5%, Cat. No AA14337G6, Alfa Aesar) and Al wires (1.0 mm dia, 99.999%, Cat. No AA10747G5, Alfa Aesar) were used as working electrodes for electrodeposition. Prior to electrodeposition, the working electrodes were sonicated in acetone for 20 min to degrease the surface and then rinsed with 18.2 MΩ cm deionized (DI) water (Millipore Quantum TEX, Cat. No QTUM0TEX1). To minimize any oxide layer on the Al surface, Al wires were further pretreated for 10 s in 5 M KOH (Potassium hydroxide pellets, Cat. No P250-3, Fisher Chemical) immediately before electrodeposition and then rinsed with DI water. During deposition, the approximate immersion depth of the wires was 2 cm. In all cases, Zn wire (1.0 mm dia, 99.95%, Cat. No AA42705G9, Alfa Aesar) and Hg/HgSO$_4$/Saturated Na$_2$SO$_4$ (CHI 151, CH Instruments) were used as the counter electrode and reference electrode, respectively. A schematic of the three-electrode electrochemical cell is shown in Figure S1a in the Supporting Information. The deposition process to make e-Zn was carried out at a current density of 143 mA cm^{-2} for 30 min in 10 mL of 1 M ZnSO$_4$ (Zinc sulfate heptahydrate, Cat. No Z68-500, Fisher Chemical). To create terraced features on the e-Zn particles, some of them were subsequently heat-treated in a tube furnace under the flow of N$_2$ gas (5.0 UHP, Praxair - ramp rate of 10°C min^{-1}) for either 24 h at 250°C or 1 h at 400°C.

Physical characterization of e-Zn

Field emission scanning electron microscopy (FESEM, Zeiss Ultra plus) was used to investigate the morphology of the electrodeposited Zn at 5 kV electron energy. X-ray diffraction (XRD) patterns were collected using a Rigaku MiniFlex II with a Cu–Kα radiation source ($\alpha = 1.5406$ Å) operated at 30 mA and 15 kV and D/teX Ultra detector between 10°–90° 2θ at a scan rate of 2° min^{-1}. Brunauer, Emmet and Teller (BET) surface area measurements were carried out using a Micromeritics ASAP 2020 with Kr as the adsorbent. Krypton was used instead of nitrogen due to its high accuracy for lower surface area (i.e., large particle) samples.

Electrochemical characterization of e-Zn on wire substrates

Discharge and cycling (charge/discharge) experiments were performed on the e-Zn (on Ni wire) working electrodes in a three-electrode electrochemical cell in both 35% KOH and 1 M ZnSO$_4$ at room temperature. Ni wire was used as the counter electrode,

while a Hg/HgO/5 M KOH (CHI 152, CH Instruments) electrode was the reference. Whatman filter paper (P8, Cat. No 09-795A, Fisher Scientific) attached to a plastic syringe was used as a separator between the counter electrode and the working electrode (Figure S1b in the Supporting Information). Potentiostatic linear sweep voltammetry (LSV) was performed in the same three-electrode cells as the discharge experiments to quantify the corrosion rate. Prior to each LSV measurement, the working electrode was equilibrated in the 35% KOH electrolyte for 30 min to stabilize the open circuit potential (OCP). Then, the LSV measurements were made at a sweep rate of 0.2 mV s^{-1} from −0.1 to 0.1 V vs. OCP. Moreover, the real-time rate of hydrogen gas evolution of e-Zn and Zn powder (Cat. No Z5-500, Fisher) was monitored by exposing the same mass of Zn (50 mg), e-Zn on Ni wire and Zn powder, to 600 μL of 35% KOH electrolyte in pressure transducer cells. Further details for pressure transducer cell construction are described later in Section 2.6.

Electrodeposition of e-Zn on Ni mesh substrate

In order to use e-Zn in coin cells or cylindrical cells, a method was needed to scale-up the electrodeposition process. Thus, e-Zn-coated mesh electrodes were prepared using a similar electrodeposition method to the wires. To do this, Ni mesh (400 nickel woven mesh sheet, Part No MO-100-0045-02) was used as the working electrode, while four Zn rods (0.5 in. dia., >99.9%, Cat. No AA00422BT, Alfa Aesar) and Hg/HgSO$_4$/Na$_2$SO$_4$(saturated) were used as the counter electrode and reference electrode, respectively, in a beaker-type cell (Figure S1c in the Supporting Information). The dimension of exposed mesh electrodes in the electrolyte was 7×6 cm^2 which resulted in 84 cm^2 geometric surface area considering both sides of the rectangular mesh. The electrodeposition was performed at 100 mA cm^{-2} by applying a constant current of 8.4 A using a current booster (Autolab Booster20 A) connected to potentiostat (Autolab PGSTAT302 N) in 160 mL of 1 M ZnSO$_4$ electrolyte.

Symmetric coin cell fabrication and testing

From the larger electrodeposited mesh, disks were cut with a geometric area of 1.76 cm^2. Symmetric cells were assembled in CR2032 coin cells (Hohsen Corp.) in air with electrolytic Zn-coated Ni mesh (e-Zn@Ni) with and without heat-treatment placed on both sides of the separator (Whatman filter paper). 40 μL of either 35% KOH or 1 M ZnSO$_4$ electrolyte was pipetted to both sides of the separator during assembly. After the spacer disk, spring, and the anodic cap of the coin cell were placed, the cell was crimped with a MTI hydraulic press (MSK-110) to a pressure of 750 PSI. For Zn foil symmetric cells, high purity Zn foil (>99.994%, Cat. No AA11913FI, Alfa Aesar) was used and the same procedure was followed.

Full cell fabrication and testing

e-Zn@Ni/MnO$_2$ full cells were assembled in cylindrical cells with the same geometry as a $\frac{1}{4}$ height AA battery, as described in our previous work.[14,18] This cell is equipped with a pressure mount that is connected to a pressure transducer (Model #MP40B-2000G, Micron Instruments) to allow the in-cell pressure to be monitored in real time during the test. To assemble the cells, a carbon nanotube ink (Tuball SWCNT 0.05% in 2-propanol) was dropped onto the inside of the steel main housing and allowed to dry. Then, a commercial EMD cathode pellet was pressed into the housing, which was then placed into a Delrin housing. Rolled separator paper (laminated cellophane) was placed into a groove at the

bottom of the Delrin housing and allowed to expand and make a contact with the cathode pellet. A tin-plated brass rod was inserted into the bottom-center of the Delrin housing and acted as the current collector. Next, 240 µL of liquid 35% KOH electrolyte was added onto the separator and vacuum was pulled to allow the electrolyte to penetrate the EMD. To use e-Zn@Ni electrodes in cylindrical cells, the larger electrodeposited mesh was cut into 4×1 cm^2 rectangles. After that, a rolled e-Zn@Ni electrode was placed into the anode column and 400 µL of 35% KOH electrolyte was added. Finally, the main chamber was enclosed using a top plate with the pressure transducer mount and the cell was sealed using bolts through the top and bottom plates.

Because the intention was to use these cells to study the rechargeability of the e-Zn@Ni anodes, the cells were intentionally anode limited. Therefore, the active material loading of the anode was lower than cathode and the N:P ratio was 0.3–0.4. e-Zn@Ni/MnO$_2$ full cells were tested at C/10 and C/20 (i.e. discharging the entire capacity of the cell in 10 h and 20 h, respectively) at three depths of discharge (DoD): 5%, 10% and 20%. Additional control experiments were done with Zn foil and Zn powder anodes, also with an EMD cathode and 35% KOH electrolyte at the same N/P ratio. The foils were used directly, in the same manner as the e-Zn mesh electrodes. The Zn powder anodes were created by mixing 400 µL of 35% KOH with ~0.3 g of Zn powder using a vortex mixer and then pipetting the resulting slurry into the anode column. Following cell assembly, constant current charge/discharge experiments were conducted to the targeted DoD with a multi-channel BT2000 Arbin battery cycler. Cycling was terminated after the discharge voltage reached to a cut-off value of 0.8 V.

2. Results and Discussion

2.1. Micron-Sized Hexagonal Shaped e-Zn Particles

In order to investigate the corrosion and reversibility of Zn surfaces, a method is needed to synthesize Zn particles with controlled structure, though lower surface area to avoid corrosion, in a single step. Electrodeposition is one such method, and it is already used to create the electrolytic manganese dioxide (EMD) used as the cathode in primary alkaline batteries. Zn electrodeposition can result in Zn particles with different morphologies,[37–38] some better than others to be employed in practical systems. Efficient Zn electrodeposition should result in non-dendritic structures as high surface area Zn dendrites are prone to rapid H$_2$ gassing. Despite the fact that electrolytic Zn preparation might have promise and be scalable, there have not been any reports of such materials shown in the literature today that lead to truly improved performance in secondary batteries with conventional chemistries.

Herein, e-Zn particles were created in a three-electrode electrochemical cell on Ni wires using a constant current electrodeposition method. The impact of current density on Zn deposition in 1 M ZnSO$_4$ electrolyte was examined and it was observed that at low current densities (i.e., < 100 mA cm^{-2}) Zn tended to grow as a film on the Ni substrate, whereas at high current densities (i.e. > 100 mA cm^{-2}) individual Zn particles with bulky structures were produced. Figure 2a–h shows SEM images after deposition in which the top and bottom row are related to low (~ 100 X) and high (~ 1000 X) magnification, respectively. At 15 mA cm^{-2} a conformal coating of Zn was produced (Figure 2a,b), whereas at 66 mA cm^{-2},
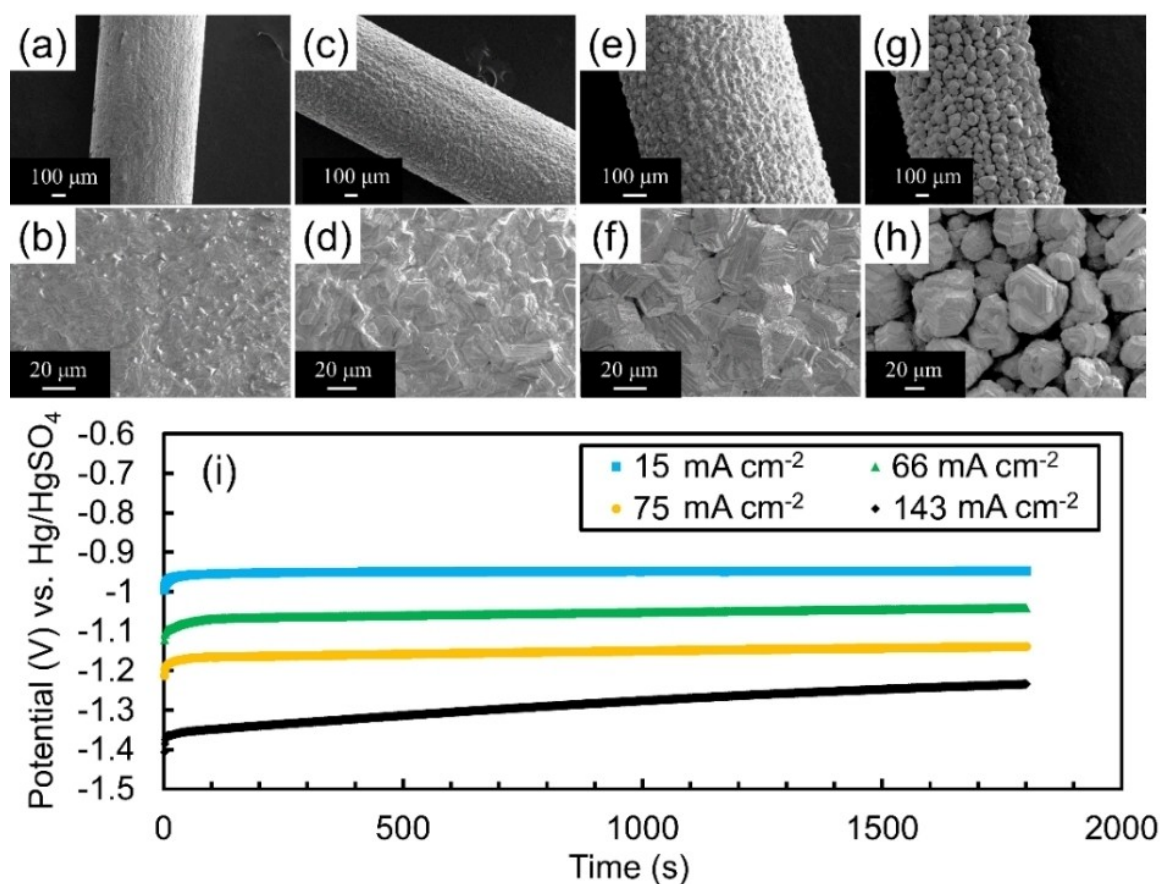

Figure 2. SEM images of e-Zn on Ni at a,b) 15 mA cm^{-2} ~17.9 C, c,d) 66 mA cm^{-2} ~61.6 C, e,f) 75 mA cm^{-2} ~89.8 C, g,h) 143 mA cm^{-2} ~163.5 C, i) potential curves during electrodeposition at different current densities.

Batteries & Supercaps

Articles
doi.org/10.1002/batt.202000112

Chemistry
Europe
European Chemical
Societies Publishing

small Zn crystallites appeared (Figure 2c,d). When the current density was further raised to 75 mA cm^{-2}, the size of the Zn crystallites was increased, and the grains became more distinct (Figure 2e,f). At a high current density of 143 mA cm^{-2}, individual particle growth was observed with pores in between (Figure 2g,h).

In addition to having a size (20–120 μm) that would be commercially preferred due to its lower surface area and ease of handling, the e-Zn particles predominantly possessed a hexagonal morphology and no dendrites were formed during electrodeposition. The corresponding potential responses during deposition at various current densities are shown in Figure 2i. The more conformal coatings resulted in a more stable and higher potential. At the highest current density, 143 mA cm^{-2}, the potential did not reach a stable value due to the pores that existed between the particles, which allowed the electrolyte to reach the underlying electrode (Ni wire) and create a mixed potential. As the current density was increased, the potentials shifted to more negative values as the kinetic overpotential increased, though the open circuit potential after deposition for all cases was the equilibrium Zn potential in the electrolyte (∼ −1.40 V vs. Hg/HgSO$_4$).

The evolution and growth of e-Zn particles on Ni was studied by varying the deposition time at a constant current density of 143 mA cm^{-2} (Figure S2 in the Supporting Information). It was seen that Zn starts to nucleate as threads (30 s) and then platelets (5 min). As the deposition time increased to 10 min, the platelets were stacked on top of each other. After 20 and 30 min deposition, the size of the particles was increased and the formation of boulder type Zn structures was initiated. After even longer deposition times, i.e., 60 min, the particles were excessively agglomerated. The effect of changing the substrate (Ni to Al) on the structure of the Zn deposits was also investigated (Figure S3 in the Supporting Information). The average mass gained and yield of Zn particles on Al was lower than that of Ni. Moreover, Zn particles on Al had tighter grain boundaries. This was evidenced not only by the SEM images, but also by the deposition potential reaching a plateau even at high current density. Additionally, there was a higher yield of particles on Ni than Al substrates. These led to the selection of Ni as the preferred substrate. Because particle-type growth (instead of conformal layer) is preferred based on the application needs, as well as the desire to compare the corrosion and discharge/charge of e-Zn to conventional Zn architectures (e.g. powder), from now on, the Zn particles formed on Ni wire at 143 mA cm^{-2} for 30 min – which resulted in the distinct, boulder-type morphology – are denoted as e-Zn for the rest of this article and were exclusively selected for further structural and electrochemical examination.

2.2. Chemical Corrosion and Electrochemical Reactivity of e-Zn Particles

Commercial Zn anodes typically employ Zn particles with oval-shaped morphologies even though Zn has a hexagonal crystal structure. This means that there are often awkward uncoordinated defects and grain boundaries that can possibly have desirable or undesirable effects. Because e-Zn particles have very well oriented hexagonal morphologies, it is possible to use them to better understand the behavior of polycrystalline particles. In particular, it is possible to study which crystallographic orientation of Zn is preferred from the perspective of balancing corrosion and discharge rates, which is an exact reflection of practical parameters such as shelf-life and accessible capacity.

Therefore, e-Zn particles were chemically corroded and electrochemically discharged in 35% KOH. Figure 3a–i shows SEM images of isolated fresh e-Zn particles as well as the Zn structures after various states of corrosion and discharge. As the corrosion

proceeds by increasing the time of exposure to 35% KOH from 1 min to 1000 min, small pits on the basal planes became increasingly visible (Figure 3b–e), while the edge planes appeared to be less affected. When discharging isolated e-Zn particles at 1 mA cm^{-2}, the dissolution also appeared to start from the basal plane (Figure 3f). At a higher rate of 10 mA cm^{-2}, basal plane dissolution happened with increased depth, while the edge-planes seemed to be intact (Figure 3g). At 15 mA cm^{-2}, the emergence of hexagonal holes on the basal plane was clear (Figure 3h). The dissolution pattern remained similar at a high rate of 20 mA cm^{-2} where the edges of the e-Zn particles were retained from the initial structure (Figure 3i). Thus, both chemical corrosion and electrochemical discharge of each individual Zn particle/grain originates from the basal plane in 35% KOH and step-edge sites appeared to be more corrosion resistant – suggesting that having more step-edge facets can be beneficial in terms of reducing the corrosion rate of Zn particles.

To be more quantitative regarding the crystallographic stability of these particles, the three major crystal planes of Zn were analyzed by XRD before and after discharge: basal plane (002) at 36.29°, prismatic plane (100) at 38.99° and pyramidal plane (101) at 43.22° (Figure 3j–k). Relative intensity calculations were done for the three major crystal planes from fitted XRD spectra with respect to a Zn source XRD pattern (03-065-3358)[39] and the relative intensity for each of the primary facets is presented in Table S1 in the Supporting Information. It was found that the relative intensities for the prismatic plane remained nearly constant after corrosion and discharge, indicating that preferential dissolution of Zn happens from basal and pyramidal planes. This is in exact agreement with the imaging results from Figure 3a–i, confirming that the step-edge does not corrode initially, whereas the basal plane and pyramidal planes do.

2.3. Effect of Zn Structure and Shape on H$_2$ Gas Evolution

Since both corrosion and dissolution of Zn originate from the basal and pyramidal planes, it is expected that e-Zn could be more corrosion resistant than conventional Zn powder (which does not have a well-defined shape) and commercial Zn. To explore the corrosion of e-Zn, conventional Zn powders and commercial Zn that are commonly used in Zn anode slurries, the H$_2$ partial pressure was monitored in real time in a closed vessel with a pressure transducer. Here, the same mass of e-Zn, Zn powder and commercial Zn were exposed to 35% KOH for 25 minutes. The surface area of e-Zn was less than the Zn powder, while the commercial Zn had a similar surface area to e-Zn (Figure S4a,b in the Supporting Information). As shown in Figure 3l, the H$_2$ gassing rate, i.e. Zn corrosion rate, was lower for e-Zn than Zn powder and commercial Zn during the 25 min corrosion experiment. It was also observed that H$_2$ gassing proceeded in two stages. There was an initial gassing event, where it is likely that small particles and surface imperfections were reacted relatively rapidly. This was followed by a slower rate, most likely the bulk corrosion rate of the material. For Zn powder, there was a very fast release of H$_2$ in the first 2 min, followed by steady corrosion over the remaining duration of the experiment. On the other hand, H$_2$ gassing for e-Zn appeared to nearly stop after the initial increase over the first 2.5 min, suggesting that the hexagonal shape, large size and low surface area of e-Zn are beneficial to reduce the Zn corrosion rate.

2.4. Effect of Heat-Treatment on the Structure and Stability of e-Zn Particles

Since step-edge planes of Zn were less active in alkaline media than basal and pyramidal planes from a chemical corrosion
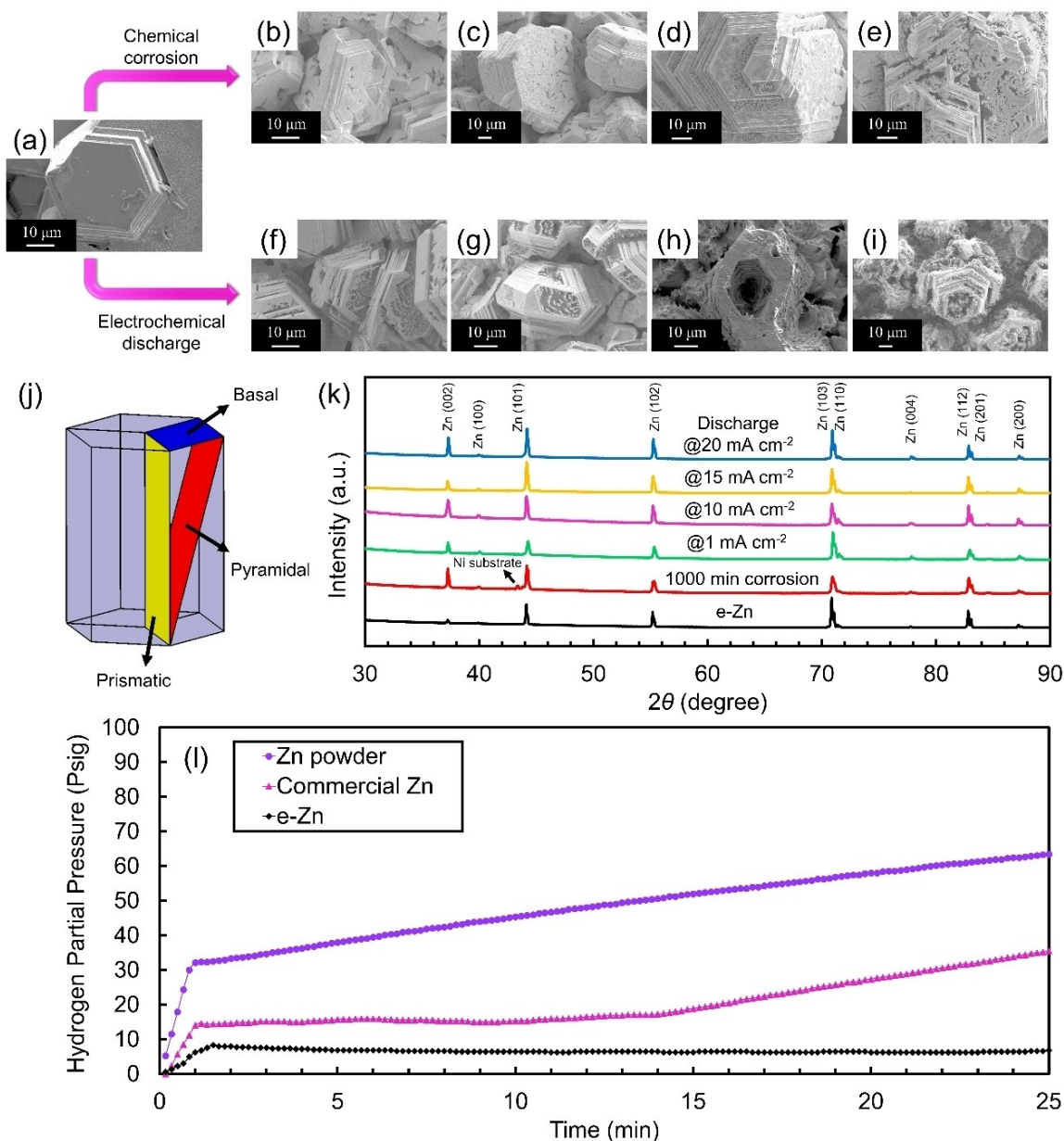
Figure 3. a) Fresh e-Zn particle on Ni substrate, b-e) chemical corrosion in 35 % KOH (b) 1 min (c) 10 min (d) 100 min (e) 1000 min; f-i) Electrochemical discharge in 35 % KOH for 30 min f) 1 mA cm^{-2}, g) 10 mA cm^{-2}, h) 15 mA cm^{-2}, i) 20 mA cm^{-2}, j) schematic representation of Zn hexagonal lattice structure, k) XRD of fresh e-Zn, after 1000 min corrosion and after discharge at different rates. l) Real time H$_2$ evolution comparison of Zn powder, commercial Zn, and e-Zn.

perspective, one pathway to further decrease the corrosion rate could be to increase the number of step-edge planes vs. basal planes. To accomplish this, the e-Zn particles were heat-treated in two ways: 1) 250 °C for 24 h; or 2) 400 °C for 1 h (which is close to the melting point of Zn, 419.5 °C). From the SEM images in Figure 4a–d it can be seen that both heat treatments resulted in the formation of terraced-type Zn (t-Zn) particles. Again, XRD (Figure S4c,d in the Supporting Information) can be used to determine the relative intensities for the three major Zn facets. It was found that the relative intensity of the basal plane, prismatic plane and pyramidal plane were changed after heat treatment compared to raw e-Zn. To be more quantitative regarding the structural changes, the texture coefficient (TC) for each facet[40] was determined using [Equation (5)] and the results are shown in Figure 4e. In [Equation (5)], $I_{(hkl)}$ is the intensity of (hkl) reflection

peak, $I_{0(hkl)}$ is the standard intensity from the Zn source XRD pattern (03-065-3358) and n is the number of reflection peaks that are taken into consideration for the analysis. If the TC is larger than one for a given facet, it means that facet has been preferentially oriented compared to a perfect infinite crystal.[33,38] It can be seen that Zn powder is randomly oriented since the TC is less than one for all three major planes. The pyramidal plane was preferentially oriented in e-Zn, whereas basal plane and pyramidal plane are preferentially developed in t-Zn. The pyramidal plane is typically attributed to the grain boundary, and, thus, the heat treatment causes the disappearance of grain boundaries and replaces it with step-edges.
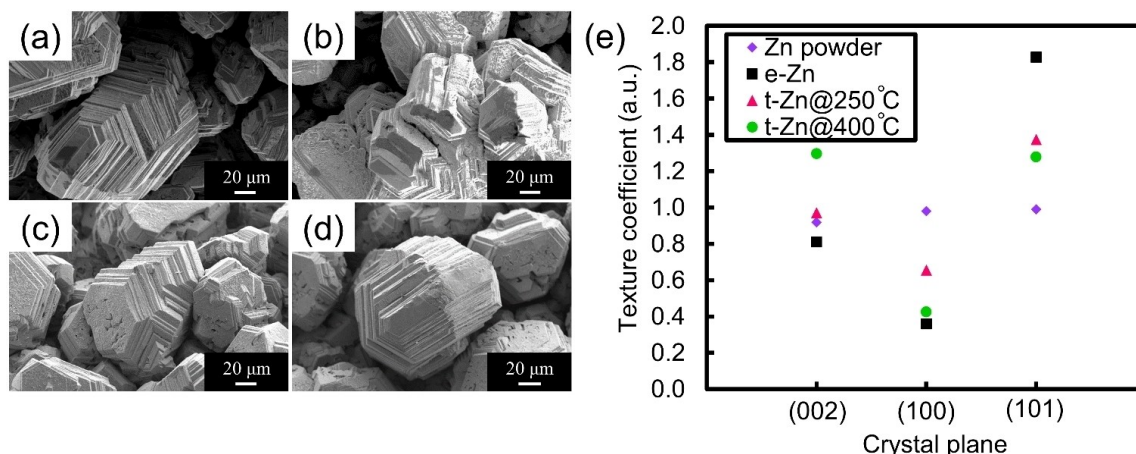
Figure 4. SEM images of heat-treated e-Zn with terraced structures (a–b) at 250 °C for 24 h (c-d) at 400 °C for 1 h (e) Texture coefficient of Zn powder, fresh e-Zn and heat-treated terraced e-Zn.

$$TC(hkl) = \frac{I_{(hkl)_i}/I_0{(hkl)_i}}{1/n \sum I_{(hkl)_n}/I_0{(hkl)_n}} \qquad (5)$$

An additional critical parameter in determining the corrosion rate of a material is the surface area, where higher surface area Zn leads to higher corrosion rates.[14,41–42] BET isotherms for e-Zn and t-Zn were collected using krypton as the working gas (Figure S5a in the Supporting Information). It was found that the e-Zn particles reported here possess significantly lower surface area (818 $cm^2 g^{-1}$) than previously reported electrodeposited Zn particles ($>$ 30,000 $cm^2 g^{-1}$).[42–43] This was confirmed by the type II isotherm, which was characteristic of a non-porous and uniform material. The heat-treatment further decreased the surface area to 767 $cm^2 g^{-1}$ for t-Zn heated at 250 °C and 695 $cm^2 g^{-1}$ for terraced Zn heated at 400 °C (Table S2 in the Supporting Information). The corrosion rate of e-Zn was lower than Zn powder as discussed previously in Section 3.3. In addition to Zn powder, it was found that the corrosion rate of e-Zn was lower than high purity Zn wire, which was compared by LSV (Figure S5b in the Supporting Information). As shown in Table 1, the corrosion rate for e-Zn (1.09×10^{-4} mg cm^{-2} min^{-1}) was 99% less than Zn wire (9.94×10^{-3} mg cm^{-2} min^{-1}). The corrosion rate was further reduced by 70% and 11% for t-Zn at 250 °C and 400 °C, respectively, compared to e-Zn. The corrosion rates were calculated based on the BET surface area values for e-Zn and t-Zn, while the geometric surface area was considered for Zn wire. These results were in agreement with a study by Sun et al. where lower corrosion current was observed for electrodeposited Zn (from 0.6 M zinc sulfate and 0.1 M ammonium sulfate electrolyte in the presence of some organic[44] and inorganic[45] additives) which appeared to have orientational order, though their electrolyte was more exotic. Hence, e-Zn and t-Zn have very high corrosion resistivity and they can be used as novel anode electrode materials with increased shelf-life in Zn-based batteries. However, for secondary battery

applications, the reversibility is also important, and thus the balance between reversibility and stability should be carefully evaluated.

2.5. Reversibility of Preferentially Oriented e-Zn Electrodes in Alkaline Media

After understanding the impact of crystallographic orientation and structural features on corrosion and discharge behavior of e-Zn at the particle-level, better matching to the true reacting environment in a larger electrode scale was needed to explore reversibility. This led to the synthesis of e-Zn on larger surface area mesh substrates instead of wires. Figure 5a shows hexagonal e-Zn particles that were deposited onto larger format Ni mesh substrates (e-Zn@Ni) in order to allow for a more realistic Zn particle loading in larger format cells. In this novel architecture, e-Zn particles are connected together, and thus, the electronic conduction throughout the electrode is increased as opposed to traditional Zn slurry anodes where Zn particles are not in continues contact with each other.[14] After punching out smaller electrodes from the larger mesh, Zn/Zn symmetric cells were constructed to examine the e-Zn and t-Zn deposition/stripping behavior at constant current charge/discharge in 35% KOH. Symmetrical cells were first cycled at 2 mA cm^{-2} for (1 h charge and 1 h discharge, equivalent to 3% DoD) and the results are shown in Figure 5b,c. e-Zn was able to cycle for 110 h (55 cycles) with overpotentials less than 40 mV ($\eta < 40$ mV), which is a fairly low overpotential and long cycle life in alkaline media compared to the literature.[46–49] For

Table 1. Measured kinetic parameters from LSV.

Sample	Corrosion potential [V vs. Hg/HgO]	Corrosion current [A cm^{-2}]	Anodic Tafel slope [V dec^{-1}]	Cathodic Tafel slope [V dec^{-1}]	Corrosion rate [mg cm^{-2} min^{-1}]
Electrolytic Zn	−1.40	5.37×10^{-6}	0.010	0.013	1.09×10^{-4}
Terraced Zn@250 °C	−1.42	1.60×10^{-6}	0.011	0.014	3.25×10^{-5}
Terraced Zn@400 °C	−1.40	4.79×10^{-6}	0.008	0.010	9.73×10^{-5}
Zn wire	−1.43	4.89×10^{-4}	0.013	0.012	9.94×10^{-3}

Batteries & Supercaps

Articles
doi.org/10.1002/batt.202000112

Chemistry Europe
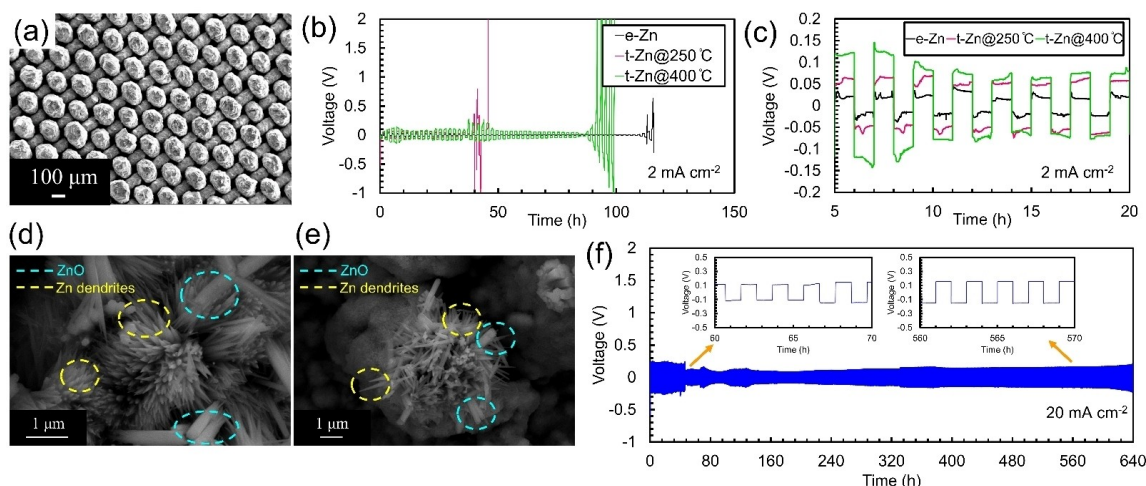European Chemical
Societies Publishing

Figure 5. a) SEM image of e-Zn on Ni mesh (e-Zn@Ni). b) Charge-discharge cycling of e-Zn and t-Zn symmetrical cells in 35% KOH at 2 mA cm^{-2}. c) Overpotential comparison of e-Zn and t-Zn in a zoomed region from 5 to 20 h. Post-cycled SEM images of d) t-Zn@250°C and e) t-Zn@400°C. f) Symmetric cell long-term cycling of e-Zn@Ni at 20 mA cm^{-2}.

example, in Pan's study, a Zn foil symmetric cell failed after only 6 cycles (~12 h), hitting a sharp polarization ($> \pm 1$ V) at 0.24 mA cm^{-2} in 40% KOH.[46] t-Zn showed larger overpotentials (Figure 5c) than e-Zn and also lower cycle life. The voltage profile for t-Zn@250°C started oscillating (larger than 0.5 V) after 20 cycles (40 h), whereas the voltage oscillation for t-Zn@400°C ($\eta > 0.5$ V) occurred after 45 cycles. The cell failure as a result of voltage oscillations was caused by the generation of H$_2$ bubbles, which may be surprising at first given that the t-Zn showed lower initial corrosion rates. However, what happened was that as the t-Zn was cycled, the reduced active area (basal plane) led to higher local current densities, premature passivation and the formation of dendrites, as can be seen in Figure 5d,e where post-cycled SEM images indicated the formation of cubic-rod shape ZnO particles as well as dendritic Zn structures with sharp tips. These types of structures for Zn dendrites and ZnO have been previously reported in the literature.[14,50–51]

The durability of e-Zn was further studied at a higher current density, 20 mA cm^{-2}, for the same discharge time (equivalent to 30% DoD). As the current density increased from 2 to 20 mA cm^{-2} in 35% KOH, the initial polarization was increased; however, the cell was stable for 320 cycles (640 h) without any obvious voltage hysteresis ($\eta < 250$ mV), Figure 5f. It is clear from the insets in Figure 5f that the cycling process was electrochemically stable due to the flat deposition and stripping profiles. The reason for long-lasting performance at higher current density is lower corrosion rate, and thus, lower H$_2$ gas generation. It is worth mentioning that dendrite growth and internal short-circuiting were suppressed here as evidenced visually. In addition, control experiments were performed using Zn foils under similar conditions and it was observed that the cells failed after only a few cycles (Figure S6 in the Supporting Information). This is in agreement with Zhang and co-workers who observed significant polarization ($> \pm 2$ V) using Zn foils in 1 M KOH, even at lower rate of 0.1 mA cm^{-2}.[47] In addition, Wang et al. showed a significant

polarization (~ ± 1 V) for cells with symmetric Zn foil electrodes in 6 M KOH at 0.2 mA cm^{-2}.[48] This suggests that e-Zn can significantly improve continuous cycling performance by mitigating corrosion.

2.6. Rechargeability of Alkaline e-Zn@Ni/MnO$_2$ Full Cells

For secondary battery applications, Zn anodes can be coupled with different cathode materials, such as various phases of MnO$_2$,[36,52–53] Ni,[22] Ag,[23–24] and V$_2$O$_5$[54] in either alkaline[55–56] or slightly acidic media.[46,57–58] Typically, alkaline electrolyte cells deliver high energy and power densities due to their conversion reaction mechanism, but limited reversibility, even at low DoD.[59] It should be noted that there are two main issues with the ways that Zn anodes are typically tested: 1) using Zn foil anodes, and/or 2) employing excess volume of electrolyte. For most studies, researchers have used simple Zn foils as anode materials to investigate novel cathode materials or electrolytes for Zn-based batteries.[35,46, 60] According to a recently published review article, 65% of all reported studies on Zn-air batteries employed Zn foil as the anode and showed significantly poorer overall performance compared to other studies that utilized Zn particles suspended in slurry or Zn sponges.[35] The reason for the poorer performance is that Zn foils have lower surface area compared to the particles, causing increased polarization. Furthermore, most researchers tested the rechargeability of Zn anodes in beaker-type cells with large volume of excess electrolyte, which is far from realistic conditions and sidesteps the complications that come with Zn passivation as it is avoided. Therefore, Electrolyte volume and Zn DoD have been determining factors in the performance of rechargeable Zn anodes, and, therefore, they need to be evaluated carefully upon cycling.[29,61]

Here, the aim was to investigate the application of e-Zn@Ni anodes in full cells with a more realistic cell architecture. Hence, commercial EMD (γ-MnO$_2$) was used as the cathode material,

which can be rechargeable at $<40\%$ of its first electron capacity,[62] though testing at 20% is most common and was chosen for this study. Anode-limited cells were assembled and the effect of Zn DoD (i.e. 5%, 10% and 20%) on the cycling performance of e-Zn@Ni/KOH/MnO$_2$ was studied at two different C-rates (i.e., C/10 and C/20). The average discharge voltage was calculated using [Equation (6)]. The average discharge voltage plays a critical role in determining the energy efficiency, which is an important consideration in commercializing a certain battery technology. The discharge cut-off voltage was set to 0.8 V.

$$V_{average}^{discharge} = \frac{1}{t_{discharge}} \int_0^{t_{discharge}} V(t)dt \qquad (6)$$

The rechargeability of e-Zn@Ni was first compared with Zn foil and Zn powder at C/20 rate and 10% DoD. As shown in Figure 6a, e-Zn@Ni had superior cycling performance, with the ability to cycle for 408 h (102 Cycles, Figure 6b). In contrast, the Zn foil and Zn powder electrodes reached the cut-off voltage of 0.8 V after 92 h (23 cycles) and 72 h (18 cycles), respectively. The inset in Figure 6a of the voltage profile also shows that the discharge and charge overpotentials were larger for Zn foil and Zn powder in comparison to e-Zn@Ni, especially Zn foil, which

was overcharged in the initial cycles. The H$_2$ evolution rate during charging was also lower for e-Zn, which is indicated by the much lower cell pressure and the less rapid increase in pressure with cycle number. The premier cycling performance of e-Zn@Ni could also be attributed to the enhanced electronic conductivity because of the contribution of the Ni as well as the connection of Zn particles throughout the network.

As expected, recharging to a lower DoD did increase cycle life. For example, at 5% DoD and a C/20 rate, the cycle life of e-Zn@Ni was increased to 356 cycles ($\sim$712 h). The pressure also increased initially, but leveled off after $\sim$300 h, oscillating between 15–20 Psig (Figure 6c). At a higher DoD of 20% and C/20 rate, the cell was only able to cycle for 120 h (15 cycles). A comparison of cycle life at C/20 rate for different Zn DoDs is provided in Figure 6d. At C/10, shown in Figure 6e, the cells were able to complete 18 ($\sim$72 h), 145 ($\sim$290 h) and 361 ($\sim$361 h) cycles at 20%, 10% and 5% DoD, respectively. The corresponding cell voltage profiles are presented in Figure S7 in the Supporting Information. Clearly, both rate and DoD are important parameters to consider for cycle life. A similar trend was observed by Ingale and co-workers where they used a similar testing protocol as this work to investigate the influence of DoD and C-rate on cycle life in Zn-MnO$_2$ cells.[63] The cycle life that was achieved using e-Zn@Ni was comparable with
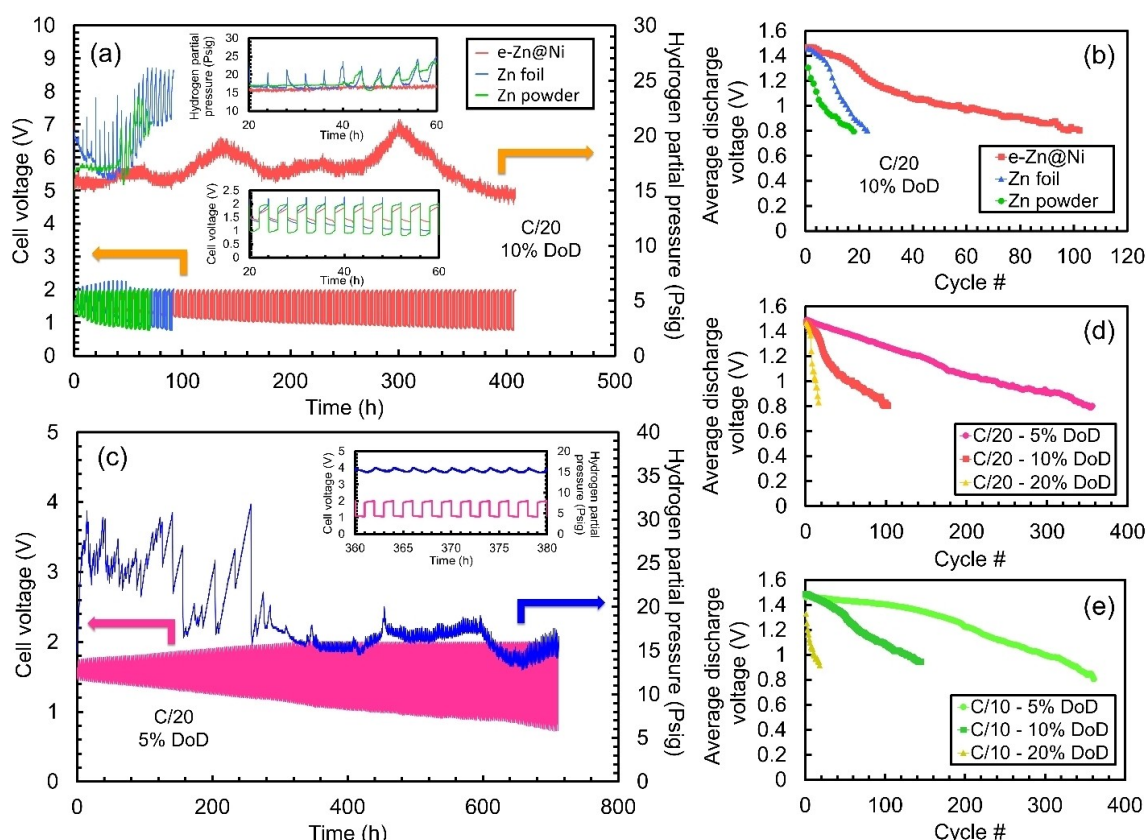

Figure 6. a) Comparison of rechargeability and H2 evolution of e-Zn@Ni with Zn foil and Zn powder anodes coupled with EMD cathode in 35% KOH at C/20 and 10% Zn DoD. b) Comparison of average discharge voltage as a function of number of cycles between e-Zn@Ni with Zn foil and Zn powder anodes coupled with EMD cathode in 35% KOH at C/20 and 10% Zn DoD. c) Rechargeability and H$_2$ evolution of e-Zn@Ni coupled with EMD cathode in 35% KOH at C/20 and 5% Zn DoD. Average discharge voltage as a function of number of cycles at 5%, 10% and 20% Zn DoD during cycling of e-Zn@Ni/35% KOH/MnO$_2$ at d) C/20 rate e) C/10 rate.

their results at 20% MnO$_2$ DoD (i.e. ~400 cycles), though they utilized a more sophisticated Zn anode by including additives and a binder. Despite the fact that e-Zn was able to outperform conventional powdered Zn, there are still improvements that can be made. Introducing electrode and electrolyte additives and binders, utilizing a gelled electrolyte and/or employing corrosion inhibitors could boost the performance of e-Zn@Ni in Zn-based alkaline battery systems including Zn-air batteries.

2.7. Reversibility of Preferentially Oriented e-Zn Electrodes in Mild Acidic Media

Another interesting modern twist on Zn-anode secondary cells has been the introduction of Zn-ion batteries that utilize mild acidic electrolytes instead of traditional alkaline electrolytes.[64–65] Here, Zn is incorporated into the cathode and plated/stripped at the anode. According to its Pourbaix diagram, the surface of Zn should be free from passivating oxide at mild pH, which is expected to improve the reversibility for Zn deposition/stripping.[36,47,52,66] The lower pH should also delay passivation as well as reduce corrosion (in mildly, not strongly, acidic electrolytes) and shape change.[54] The dendrite formation mechanism is also anticipated to be different from alkaline electrolytes, because Zn^{2+} ions act as the charge carriers in mild acidic media instead of zincate ions. However, whether Zn dendrites form in mild aqueous electrolytes in Zn-ion batteries or not, is still controversial. Recently, Yang et al. reported the formation of Zn dendrites in a Zn-ion battery at high current densities (~10 mA cm^{-2}), but not at low current densities (~1 mA cm^{-2}).[50] Since the standard redox potential of Zn/Zn^{2+} (−0.76 V vs SHE) is below the H$_2$ evolution potential (0 V vs SHE) in mild acidic media, H$_2$ evolution is also thermodynamically favorable. Despite the possibility for dendrite formation, corrosion and H$_2$ gas evolution at mild pH, ZnSO$_4$ based electrolytes have shown better reversibility in symmetric cells compared to alkaline KOH. For example, Zhang et al. reported that Zn foil plating/stripping in symmetric cells can survive 25 cycles (50 h) at 0.1 mA cm^{-2} with overpotentials less than ±0.1 V in 3 M ZnSO$_4$, while in 1 M KOH the cell failed after the first cycle by reaching to ±2 V overpotential.[47] Therefore, Zn electrodes behave differently in mild acidic media. Yet, the influence of the Zn electrode structure/architecture on the reversibility has not been well-studied in mild acidic media.

Given that the deposition electrolyte used in our study to synthesize e-Zn was 1 M ZnSO$_4$, it is possible that starting with e-Zn particles might be able to improve the reversible performance of such cells. In other words, there could be a synergistic effect between the synthesized electrolytic Zn technique and reversible deposition/stripping of Zn that impacts the reversibility. In order to investigate this phenomenon, first e-Zn particles deposited on a Ni wire substrate were discharged and cycled in a three-electrode cell configuration with excess electrolyte and the structural changes were compared in 1 M ZnSO$_4$ and 35% KOH electrolytes. Then, the reversibility of e-Zn@Ni mesh electrodes was studied in symmetric coin cell

geometry with a known volume of 1 M ZnSO$_4$ electrolyte and compared with 35% KOH alkaline electrolyte.

The e-Zn particles on Ni wire were discharged at current densities of 1, 2, 5, 10, 20 and 50 mA cm^{-2} for 30 min. It was found that the Zn particles better retained their structures – even at high current densities – in 1 M ZnSO$_4$ (Figure S8 in the Supporting Information) than they did in 35% KOH (Figure 3f–i). In KOH, Zn dissolution was initiated from the basal plane just after discharge, causing particle collapse. Recharging in 35% KOH at 0.2 and 2 mA cm^{-2} also resulted in the growth of some mossy structures on the basal plane (Figure S9 in the Supporting Information). However, the behavior of e-Zn in 1 M ZnSO$_4$ was very different. Here, small platelet-type Zn structures formed during cycling while the overall hexagonal shape of the particles was mostly unchanged.

Next, the reversibility of e-Zn@Ni was tested in symmetric coin cells using 1 M ZnSO$_4$ electrolyte. The cycling performance of a symmetric e-Zn@Ni cell at 2 mA cm^{-2} is shown in Figure 7a. The e-Zn@Ni electrodes were able to cycle 1000 times (2000 h) in 1 M ZnSO$_4$ with $\eta < 250$ mV (the test was programmed to terminate after 1000 cycles), which is far superior performance compared to 35% KOH due to much less corrosion and H$_2$ gassing. At a high rate of 20 mA cm^{-2} in 1 M ZnSO$_4$, the cell showed $\eta < 300$ mV after 345 cycles (690 h) (Figure 7b), though the overpotential did increase gradually to ($>\pm 1$ V) at ~700 h resulting in cell failure. After the initial cycling, the cells shown in Figure 7a,b were rested for a day to investigate the reversible behavior after recovery from continuous cycling. It can be seen that after rest, the polarization went down initially and then increased slowly. The reason for this behavior could be the recovery of Zn from the discharged state, which increases the Zn utilization in comparison with continuous cycling, as well as the removal of some H$_2$ bubbles from the electrode surface.

The products of post-cycled e-Zn symmetric cells were characterized by XRD (Figure 7c). It was found that the diffraction peaks related to polycrystalline Zn were present in all cases and the peak intensities were higher after cycling in 1 M ZnSO$_4$ compared to 35% KOH, which confirmed that Zn could better retain its structure after cycling in mild acidic electrolyte compared to alkaline electrolyte. Moreover, the peaks related to ZnO were observed in both 35% KOH and 1 M ZnSO$_4$. Different hydration states of zinc sulfate hydroxide precipitates, i.e., Zn$_4$SO$_4$(OH)$_6 \cdot n$H$_2$O were also found in post-cycled electrodes in 1 M ZnSO$_4$. The reaction mechanism for the formation of Zn$_4$SO$_4$(OH)$_6 \cdot n$H$_2$O in full cells employing Zn anodes and ZnSO$_4$ electrolyte has been proposed previously.[46,67–69] However, in this work, it was found that Zn$_4$SO$_4$(OH)$_6$, Zn$_4$SO$_4$(OH)$_6 \cdot$H$_2$O and Zn$_4$SO$_4$(OH)$_6 \cdot$5H$_2$O are formed in symmetric cells and were found in both the charged and discharged state in symmetric cells without pairing to a cathode material in full cell. The corresponding SEM images of e-Zn@Ni in both 35% KOH and 1 M ZnSO$_4$ at 20 mA cm^{-2} are shown in Figure 7d–k. In 35% KOH, the formation of secondary Zn structures with needle-type shapes as well as passivated ZnO structures can be seen on both the anode side and cathode side.[14] Positively, in 1 M ZnSO$_4$, e-Zn particles were able to mostly maintain their structure and have a longer cycle life than other proposed Zn anodes to date. This suggests that e-
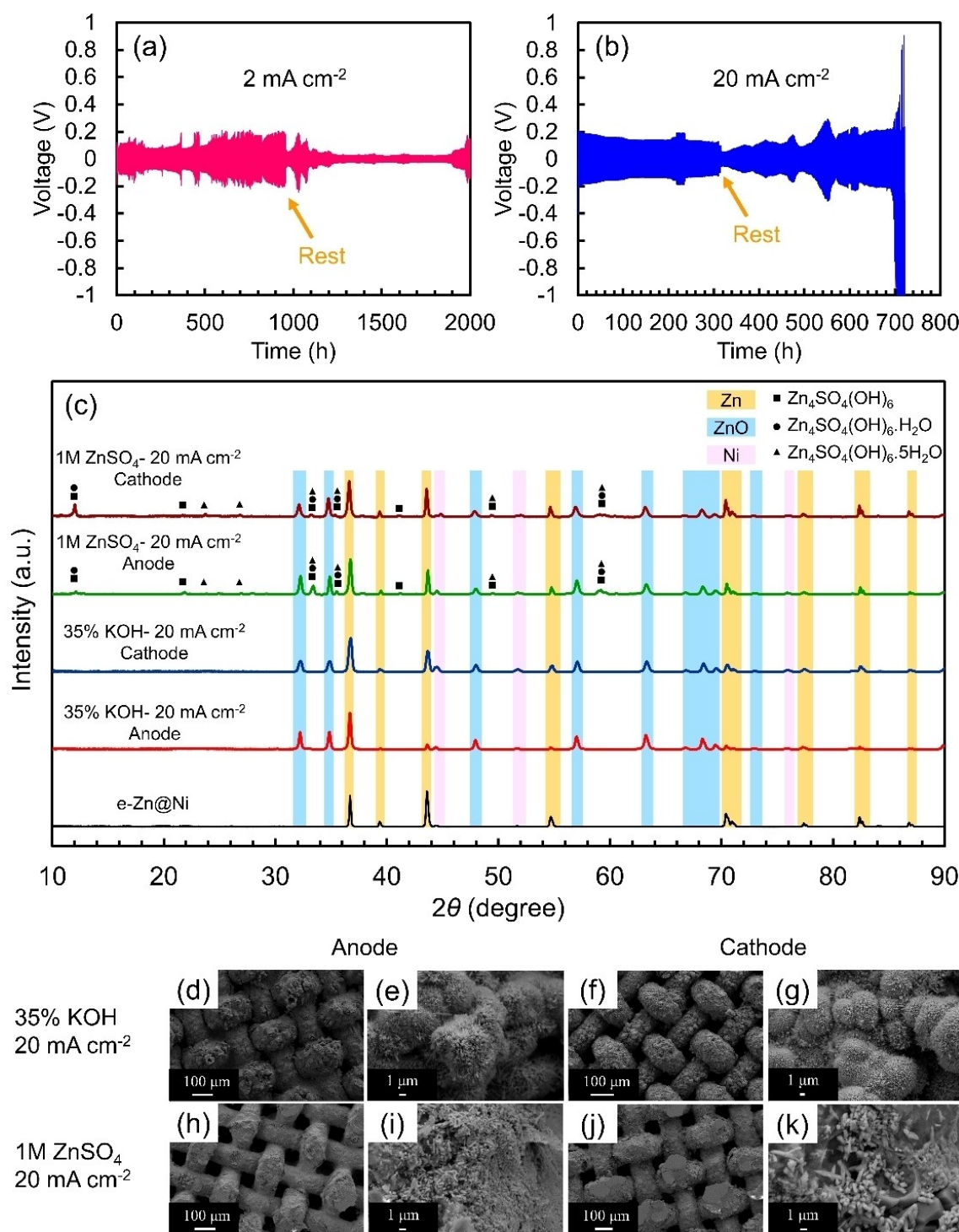
Batteries & Supercaps

Articles
doi.org/10.1002/batt.202000112

Chemistry Europe
European Chemical
Societies Publishing

Figure 7. Charge-discharge cycling of Zn/Zn symmetrical cell using e-Zn@Ni in 1 M ZnSO$_4$ at a) 2 mA cm^{-2} (equivalent to 3% DoD), b) 20 mA cm^{-2} (equivalent to 30% DoD). c) XRD patterns of fresh e-Zn@Ni and post-cycled e-Zn@Ni at 20 mA cm^{-2} in 35% KOH and 1 M ZnSO$_4$ for both anode and cathode electrodes. SEM images of post-cycled e-Zn@Ni at 20 mA cm^{-2} in d,e) 35% KOH anode side, f,g) 35% KOH cathode side, h,i) 1 M ZnSO$_4$ anode side, j,k) 1 M ZnSO$_4$ cathode side.

Zn might result in a very high performing Zn-ion battery if paired with a suitable cathode material, though it should be noted that there are still serious problems on the cathode side of Zn-ion batteries that must be solved before practical cells can be achieved.[34,70]

3. Conclusions

In this work, novel ~100 micron preferentially oriented Zn anodes were created with large size and low H$_2$ gassing rate. Different characteristics of these e-Zn particles were investigated, and it was found that the prismatic (edge) planes are

Batteries & Supercaps

Articles
doi.org/10.1002/batt.202000112

Chemistry
Europe
European Chemical
Societies Publishing

more corrosion resistant in alkaline media. Moreover, the e-Zn particles showed very stable reversibility with low overpotentials in symmetric cells at a high rate of 20 mA cm^{-2} for 320 cycles in 35% KOH. Furthermore, in anode-limited alkaline full cells with simultaneous real time H$_2$ evolution measurement, e-Zn@Ni demonstrated far superior reversibility and cycle life as well as lower corrosion rate compared to Zn powder and Zn foil. Finally, applying the e-Zn particles to an electrolyte relevant to emerging Zn-ion batteries showed excellent performance, including no dendrite formation upon cycling, low overpotentials (typically < 0.2 V) and long cycle life without failure (2000 cycles) under certain conditions. The findings of this study show that e-Zn is a very promising material that can be implemented to enhance a wide variety of applications including alkaline Zn, Zn-air and Zn-ion batteries.

Acknowledgements

Conflict of Interest

The authors declare no conflict of interest.

[1] Y. Liu, Y. Zhu, Y. Cui, *Nat. Energy* **2019**, *4*, 540–550.
[2] B. Ng, X. Peng, E. Faegh, W. E. Mustain, *J. Mater. Chem. A* **2020**, *8*, 2712–2727.
[3] Q. Wang, L. Jiang, Y. Yu, J. Sun, *Nano Energy* **2019**, *55*, 93–114.
[4] B. Ng, P. T. Coman, E. Faegh, X. Peng, S. G. Karakalos, X. Jin, W. E. Mustain, R. E. White, *ACS Appl. Energy Mater.* **2020**, *3*, 3653–3664.
[5] J. Fu, Z. P. Cano, M. G. Park, A. Yu, M. Fowler, Z. Chen, *Adv. Mater.* **2017**, *29*, 1604685.
[6] X. Chen, Z. Zhou, H. E. Karahan, Q. Shao, L. Wei, Y. Chen, *Small* **2018**, *14*, 1801929.
[7] J. Yi, P. Liang, X. Liu, K. Wu, Y. Liu, Y. Wang, Y. Xia, J. Zhang, *Energy Environ. Sci.* **2018**, *11*, 3075–3095.
[8] Z. Zhao, X. Fan, J. Ding, W. Hu, C. Zhong, J. Lu, *ACS Energy Lett.* **2019**, *4*, 2259–2270.
[9] V. Yufit, F. Tariq, D. S. Eastwood, M. Biton, B. Wu, P. D. Lee, N. P. Brandon, *Joule* **2019**, *3*, 485–502.
[10] Y. Yamada, J. Wang, S. Ko, E. Watanabe, A. Yamada, *Nat. Energy* **2019**, *4*, 269–280.
[11] M. R. Lukatskaya, J. I. Feldblyum, D. G. Mackanic, F. Lissel, D. L. Michels, Y. Cui, Z. Bao, *Energy Environ. Sci.* **2018**, *11*, 2876–2883.
[12] S. Chen, R. Lan, J. Humphreys, S. Tao, *Energy Storage Mater.* **2020**.
[13] B. W. Olbasa, F. W. Fenta, S.-F. Chiu, M.-C. Tsai, C.-J. Huang, B. A. Jote, T. T. Beyene, Y.-F. Liao, C.-H. Wang, W.-N. Su, *ACS Appl. Energy Mater.* **2020**.
[14] E. Faegh, T. Omasta, M. Hull, S. Ferrin, S. Shrestha, J. Lechman, D. Bolintineanu, M. Zuraw, W. E. Mustain, *J. Electrochem. Soc.* **2018**, *165*, A2528–A2535.
[15] Y. Xiao, J. Shi, F. Zhao, Z. Zhang, W. He, *J. Electrochem. Soc.* **2018**, *165*, A47–A54.
[16] J. Huang, Z. Yang, R. Wang, Z. Zhang, Z. Feng, X. Xie, *J. Mater. Chem. A* **2015**, *3*, 7429–7436.
[17] J. Hao, J. Long, B. Li, X. Li, S. Zhang, F. Yang, X. Zeng, Z. Yang, W. K. Pang, Z. Guo, *Adv. Funct. Mater.* **2019**, 1903605.
[18] E. Faegh, S. Shrestha, X. Zhao, W. E. Mustain, *J. Appl. Electrochem.* **2019**, 1–13.
[19] M. Gong, Y. Li, H. Zhang, B. Zhang, W. Zhou, J. Feng, H. Wang, Y. Liang, Z. Fan, J. Liu, *Energy Environ. Sci.* **2014**, *7*, 2025–2032.
[20] A. R. Mainar, L. C. Colmenares, J. A. Blázquez, I. Urdampilleta, *Int. J. Energy Res.* **2018**, *42*, 903–918.
[21] Y. Li, H. Dai, *Chem. Soc. Rev.* **2014**, *43*, 5257–5275.
[22] J. F. Parker, C. N. Chervin, I. R. Pala, M. Machler, M. F. Burz, J. W. Long, D. R. Rolison, *Science* **2017**, *356*, 415–418.
[23] J. F. Parker, C. N. Chervin, E. S. Nelson, D. R. Rolison, J. W. Long, *Energy Environ. Sci.* **2014**, *7*, 1117–1124.
[24] J. S. Ko, A. B. Geltmacher, B. J. Hopkins, D. R. Rolison, J. W. Long, J. F. Parker, *ACS Appl. Energy Mater.* **2018**, *2*, 212–216.
[25] M. Li, J. Meng, Q. Li, M. Huang, X. Liu, K. A. Owusu, Z. Liu, L. Mai, *Adv. Funct. Mater.* **2018**, *28*, 1802016.
[26] D. Stock, S. Dongmo, K. Miyazaki, T. Abe, J. Janek, D. Schröder, *J. Power Sources* **2018**, *395*, 195–204.
[27] Y. Zeng, X. Zhang, R. Qin, X. Liu, P. Fang, D. Zheng, Y. Tong, X. Lu, *Adv. Mater.* **2019**, *31*, 1903675.
[28] D. Chao, W. Zhou, C. Ye, Q. Zhang, Y. Chen, L. Gu, K. Davey, S. Z. Qiao, *Angew. Chem. Int. Ed.* **2019**, *58*, 7823–7828.
[29] M. Chamoun, B. J. Hertzberg, T. Gupta, D. Davies, S. Bhadra, B. Van Tassell, C. Erdonmez, D. A. Steingart, *NPG Asia Mater.* **2015**, *7*, e178.
[30] D. E. Turney, J. W. Gallaway, G. G. Yadav, R. Ramirez, M. Nyce, S. Banerjee, Y.-C. K. Chen-Wiegart, J. Wang, M. J. D'Ambrose, S. Kolhekar, *Chem. Mater.* **2017**, *29*, 4819–4832.
[31] T.-H. Wu, Y. Zhang, Z. D. Althouse, N. Liu, *Materials Today Nano* **2019**, 100032.
[32] Z. Liu, T. Cui, G. Pulletikurthi, A. Lahiri, T. Carstens, M. Olschewski, F. Endres, *Angew. Chem. Int. Ed.* **2016**, *55*, 2889–2893; *Angew. Chem.* **2016**, *128*, 2939–2943.
[33] D. H. Won, H. Shin, J. Koh, J. Chung, H. S. Lee, H. Kim, S. I. Woo, *Angew. Chem. Int. Ed.* **2016**, *55*, 9297–9300; *Angew. Chem.* **2016**, *128*, 9443–9446.
[34] B. Tang, L. Shan, S. Liang, J. Zhou, *Energy Environ. Sci.* **2019**, *12*, 3288–3304.
[35] D. Stock, S. Dongmo, J. R. Janek, D. Schröder, *ACS Energy Lett.* **2019**, *4*, 1287–1300.
[36] J. Huang, Z. Guo, Y. Ma, D. Bin, Y. Wang, Y. Xia, *Small Methods* **2019**, *3*, 1800272.
[37] C.-C. Yang, S.-J. Lin, *J. Power Sources* **2002**, *112*, 174–183.
[38] D. Desai, X. Wei, D. A. Steingart, S. Banerjee, *J. Power Sources* **2014**, *256*, 145–152.
[39] E. R. Jette, F. Foote, *J. Chem. Phys.* **1935**, *3*, 605–616.
[40] M. Shimizu, K. Hirahara, S. Arai, *Phys. Chem. Chem. Phys.* **2019**, *21*, 7045–7052.
[41] Y.-D. Cho, G. T.-K. Fey, *J. Power Sources* **2008**, *184*, 610–616.
[42] B. Sharifi, M. Mojtahedi, M. Goodarzi, J. V. Khaki, *Hydrometallurgy* **2009**, *99*, 72–76.
[43] S. Ullah, A. Badshah, F. Ahmed, R. Raza, A. A. Altaf, R. Hussain, **2011**.
[44] K. E. Sun, T. K. Hoang, T. N. L. Doan, Y. Yu, X. Zhu, Y. Tian, P. Chen, *ACS Appl. Mater. Interfaces* **2017**, *9*, 9681–9687.
[45] K. E. Sun, T. K. Hoang, T. N. L. Doan, Y. Yu, P. Chen, *Chemistry–A European Journal* **2018**, *24*, 1667–1673.
[46] H. Pan, Y. Shao, P. Yan, Y. Cheng, K. S. Han, Z. Nie, C. Wang, J. Yang, X. Li, P. Bhattacharya, *Nat. Energy* **2016**, *1*, 16039.
[47] N. Zhang, F. Cheng, Y. Liu, Q. Zhao, K. Lei, C. Chen, X. Liu, J. Chen, *J. Am. Chem. Soc.* **2016**, *138*, 12894–12901.
[48] F. Wang, O. Borodin, T. Gao, X. Fan, W. Sun, F. Han, A. Faraone, J. A. Dura, K. Xu, C. Wang, *Nat. Mater.* **2018**, *17*, 543.
[49] N. Zhang, F. Cheng, J. Liu, L. Wang, X. Long, X. Liu, F. Li, J. Chen, *Nat. Commun.* **2017**, *8*, 1–9.
[50] Q. Yang, G. Liang, Y. Guo, Z. Liu, B. Yan, D. Wang, Z. Huang, X. Li, J. Fan, C. Zhi, *Adv. Mater.* **2019**, *31*, 1903778.
[51] Y. Zhang, Y. Wu, W. You, M. Tian, P. W. Huang, Y. Zhang, Z. Sun, Y. Ma, T. Hao, N. Liu, *Nano Lett.* **2020**.
[52] J. Ming, J. Guo, C. Xia, W. Wang, H. N. Alshareef, *Mater. Sci. Eng. R* **2019**, *135*, 58–84.
[53] C. Xie, T. Li, C. Deng, Y. Song, H. Zhang, X. Li, *Energy Environ. Sci.* **2020**, *13*, 135–143.
[54] D. Kundu, B. D. Adams, V. Duffort, S. H. Vajargah, L. F. Nazar, *Nat. Energy* **2016**, *1*, 16119.
[55] G. G. Yadav, X. Wei, J. Huang, J. W. Gallaway, D. E. Turney, M. Nyce, J. Secor, S. Banerjee, *J. Mater. Chem. A* **2017**, *5*, 15845–15854.

[56] G. G. Yadav, J. W. Gallaway, D. E. Turney, M. Nyce, J. Huang, X. Wei, S. Banerjee, *Nat. Commun.* **2017**, *8*, 14424.

[57] M. H. Alfaruqi, V. Mathew, J. Gim, S. Kim, J. Song, J. P. Baboo, S. H. Choi, J. Kim, *Chem. Mater.* **2015**, *27*, 3609–3620.

[58] A. S. Poyraz, J. Laughlin, Z. Zec, *Electrochim. Acta* **2019**, *305*, 423–432.

[59] G. G. Yadav, J. Cho, D. Turney, B. Hawkins, X. Wei, J. Huang, S. Banerjee, M. Nyce, *Adv. Energy Mater.* **2019**, *9*, 1902270.

[60] Y. Li, M. Gong, Y. Liang, J. Feng, J.-E. Kim, H. Wang, G. Hong, B. Zhang, H. Dai, *Nat. Commun.* **2013**, *4*, 1805.

[61] J. F. Parker, J. S. Ko, D. R. Rolison, J. W. Long, *Joule* **2018**, *2*, 2519–2527.

[62] G. G. Yadav, D. Turney, J. Huang, X. Wei, S. Banerjee, *ACS Energy Lett.* **2019**, *4*, 2144–2146.

[63] N. D. Ingale, J. W. Gallaway, M. Nyce, A. Couzis, S. Banerjee, *J. Power Sources* **2015**, *276*, 7–18.

[64] J. Wang, J.-G. Wang, H. Liu, C. Wei, F. Kang, *J. Mater. Chem. A* **2019**, *7*, 13727–13735.

[65] J. Wang, J.-G. Wang, H. Liu, Z. You, C. Wei, F. Kang, *J. Power Sources* **2019**, *438*, 226951.

[66] A. Konarov, N. Voronina, J. H. Jo, Z. Bakenov, Y.-K. Sun, S.-T. Myung, *ACS Energy Lett.* **2018**, *3*, 2620–2640.

[67] M. Chamoun, W. R. Brant, C.-W. Tai, G. Karlsson, D. Noréus, *Energy Storage Mater.* **2018**, *15*, 351–360.

[68] B. Lee, H. R. Seo, H. R. Lee, C. S. Yoon, J. H. Kim, K. Y. Chung, B. W. Cho, S. H. Oh, *ChemSusChem* **2016**, *9*, 2948–2956.

[69] D. Kundu, S. H. Vajargah, L. Wan, B. Adams, D. Prendergast, L. F. Nazar, *Energy Environ. Sci.* **2018**, *11*, 881–892.

[70] C. Li, X. Zhang, W. He, G. Xu, R. Sun, *J. Power Sources* **2020**, *449*, 227596.